Available online at www.sciencedirect.com
ScienceDirect
Trans. Nonferrous Met. Soc. China 35(2025) 1045−1056
Transactions of Nonferrous Metals Society of China
www.tnmsc.cn

Microstructure and mechanical properties of selective laser melting Al−Mg−Mn−Sc−Zr alloy annealed at different temperatures

Yao LI[1], Guo-fu XU[1,2], Xiao-yan PENG[1,2], Ying DENG[1,2], Zhi-min YIN[1,2]

1. School of Materials Science and Engineering, Central South University, Changsha 410083, China;
2. Key Laboratory of Nonferrous Materials Science and Engineering of Ministry of Education, Central South University, Changsha 410083, China

Received 1 March 2024; accepted 25 March 2025

Abstract: Al−3.51Mg−0.42Mn−0.76Sc−0.40Zr (wt.%) alloy was prepared by selective laser melting (SLM) method. The mechanical properties and microstructure of the alloy after annealing at 300 °C or 325 °C for 6 h were studied. The tensile strength, yield strength and elongation of the SLM alloy were 339 MPa, 213 MPa and 24%, respectively. After annealing at 300 °C for 6 h, the tensile and yield strength of the alloy were increased to 518 MPa and 505 MPa, respectively, and the elongation decreased to 13%. After annealing at 325 °C for 6 h, the yield strength of the alloy was reduced to 483 MPa. The grain size of the alloy after annealing at 300 °C and 325 °C did not grow significantly, but the segregation of Mg element was significantly reduced. Nanoscale Al_3(Sc,Zr) phase was precipitated from the alloy matrix, and its average size increased with the increase of annealing temperature. Therefore, the strength improvement of the annealed SLM aluminum alloy was mainly attributed to the precipitation strengthening of Al_3(Sc,Zr), and the strengthening mechanism was mainly dislocation cutting mechanism. When the annealing temperature was too high, the coarsening of Al_3(Sc,Zr) particles caused the strength to decrease.

Key words: Al−Mg−Mn−Sc−Zr alloy; selective laser melting; annealing temperature; microstructure; mechanical property

1 Introduction

In recent years, with the continuous research and innovation in the field of 3D printing scientific research, 3D printing metal-based Al alloy materials have begun to develop worldwide and market-orientedly. Therefore, the application in the industrial fields faces higher challenges to the combination of design and manufacturing, as well as the combination of structure and function. As a typical additive manufacturing technology, selective laser melting (SLM) forming has become an effective way to solve the problems of manufacturing lightweight, functional optimization, complex geometric structure and high-performance Al alloy components [1−3], which can be used to accurately fabricate metal parts layer by layer (Fe, Ni, Al, Ti, etc) [4−7]. Compared with other traditional processing methods (for example, casting [8], stamping [9], extrusion [10] and rolling [11]), SLM has more advantages, including fine microstructure, superior mechanical properties, short processing cycle and easy formability [12,13]. However, considering the special characteristics of aluminum alloy, such as low melting point, high thermal conductivity and high laser reflectivity, it is harder to manufacture Al alloy parts by SLM than other materials [14,15].

SLM forming technology has received extensive

Corresponding author: Xiao-yan PENG, Tel: +86-15111032048, E-mail: pxy0807@126.com
DOI: https://doi.org/10.1016/S1003-6326(24)66733-6

attention. For example, MA et al [16] studied the effect of bimodal microstructure on the tensile properties of SLM Al−Mg−Sc−Zr alloy, who found that the strengthening effect of the alloy caused by SLM was mainly attributed to the grain boundary. WANG et al [17] studied the strength−plasticity synergy of SLM Al−Mg−Sc−Zr alloys, and found that the strain distribution between equiaxed crystals and columnar crystals can simultaneously improve the strength and toughness. SHI et al [18] studied the effect of adding Sc on Al−Mg−Zr alloys, and found that the alloy containing 0.2 wt.% Zr did not emerge mixed crystal structure, while the alloy with 1.0wt.% Sc presented a mixed one consisting of coarse columnar crystals and fine equiaxed crystals, both of which were the unique characteristics of SLM prepared Al alloys compared to Al alloys prepared with traditional methods, possessing the ability to effectively adjust the strength and toughness of the alloy. A Ti-modified SLM Al−Cu−Mg alloy was investigated by ZHANG et al [19]. It was found that the Al_3Ti precipitates formed a heterogeneous phase nuclei in Ti-containing alloys, which promoted grain refinement and columnar to equiaxed transformation, eliminated hot tear cracks, and improved the properties of the alloy. In addition, ZHANG et al [2] also studied the process, structure, properties and development trend of SLM aluminum alloys. Studies showed that high levels of residual stress and metallurgical defects such as spheroidization, porosity, and cracks were prevalent in SLM-fabricated aluminum alloys, which not only reduced surface roughness and dimensional accuracy, but also led to poor mechanical properties. However, the changes in structure and properties of Al alloys manufactured by SLM after annealing at different temperatures in the later stage are closely related to the effects of alloying elements (Sc, Zr, etc). In addition, the mechanism of the effect of annealing temperature on the microstructure and properties of SLM alloys has less been studied.

This study mainly focused on the evolution of the microstructure and mechanical properties of the Al alloy manufactured by SLM after annealing at different temperatures. Specifically, the role of alloying elements, such as Sc and Zr in the annealing process at different temperatures will be given out.

2 Experimental

The material used in this paper was Al−Mg−Mn−Sc−Zr alloy prepared by FS271M laser selective melting equipment, with a chemical composition of Al−3.51Mg−0.42Mn−0.76Sc−0.40Zr (wt.%). In order to study the effect of annealing treatment on microstructure and tensile properties of SLM alloys, the SLM alloys were annealed at different temperatures (300 °C and 325 °C for 6 h) using a high-temperature resistance furnace. The room temperature tensile test was operated on the MTS810 tensile testing machine and the stretching speed was 2 mm/min. There were three sets of parallel samples of each state, and the result was the average of three samples.

The morphology of the tensile fracture was observed on a Sirion 200 field emission scanning electron microscope (SEM) with an operating voltage of 20 kV. The JXA-8230 electron probe microanalyzer (EPMA) was used to observe alloying element distribution. The microstructure was observed on an FEI Tecnai G2F20 transmission electron microscope (TEM) by a high- angle annular dark-field (HAADF) imaging mode with an acceleration voltage of 200 kV. The sample was first mechanically thinned to about 80 μm, and a *d*3 mm disc was punched out of the thinned sample. The samples were then thinned by electrolytic double spray on the MTP-1 device. The electrolyte was a mixed solution of CH_3OH and HNO_3 (volume ratio of 3∶1), the working voltage was 10−15 V and the current was 60−80 mA in the temperature range of −30 to −20 °C. The morphology of the grains was observed by electron backscatter diffractometer (EBSD) on the Sirion 200 field emission scanning electron microscope. After mechanical polishing, the EBSD sample was electrolytically polished in a mixed solution of perchloric acid and ethanol (volume ratio of 1∶9) at 15 V, and the temperature was controlled below −20 °C. The test data was analyzed using a TSL OIM software.

3 Results

3.1 EPMA characterization

Figure 1 shows the distribution of alloy elements of the alloy in the SLM state and after annealing at

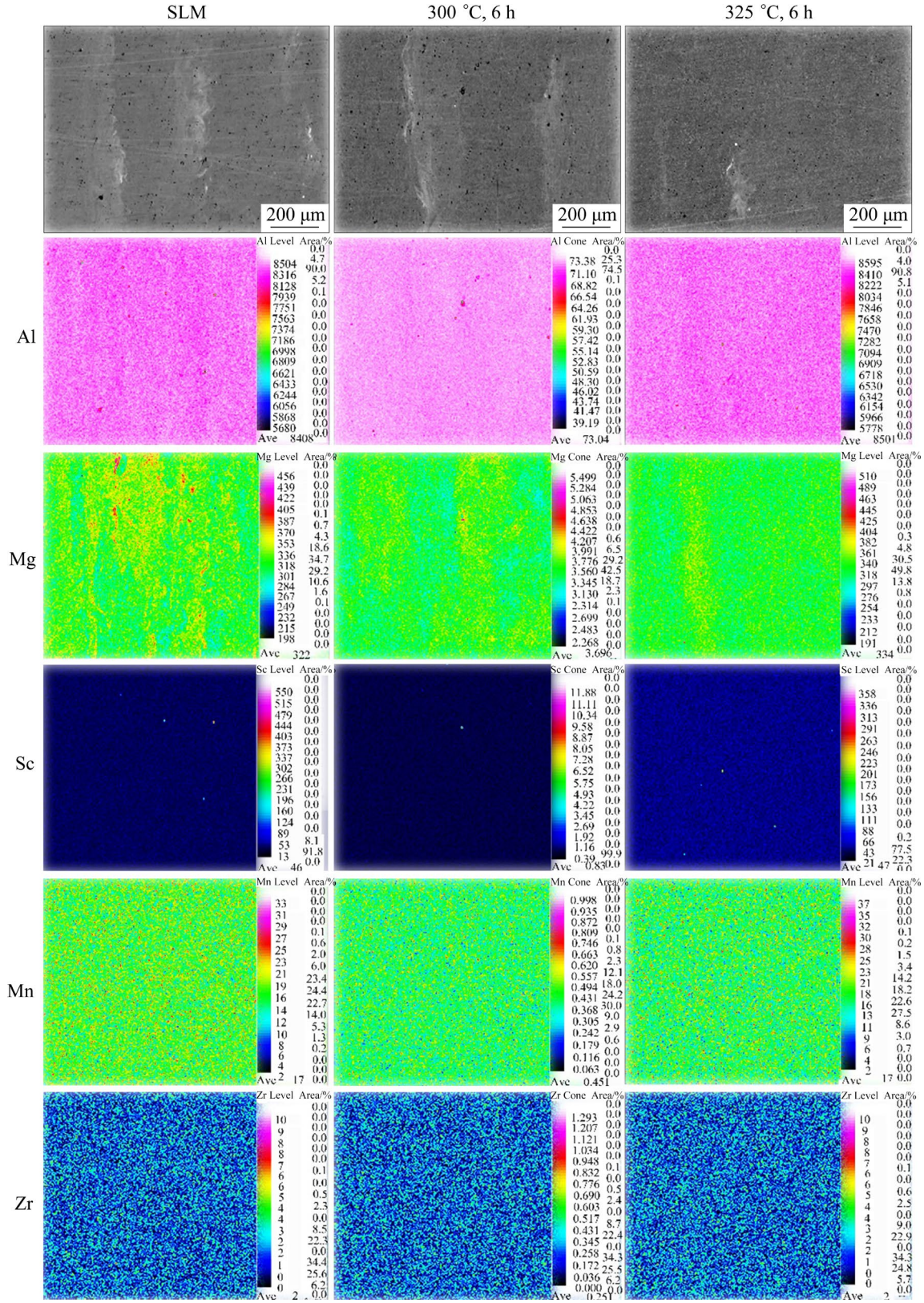

Fig. 1 Element distribution map of SLM alloy with different annealing treatments

different temperatures. Obvious segregation of Mg could be found in the SLM sample, while other elements are evenly distributed in the Al matrix. However, the element segregation phenomenon on the surface of samples was gradually reduced after annealing of 300 °C, 6 h and 325 °C, 6 h, but there is a small amount of Mg element segregation after annealing of 300 °C, 6 h.

3.2 TEM observation

Figure 2 presents the scanning transmission electron microscopy (STEM) images of the alloy in SLM state and annealing state. It can be seen that the microstructures of all the samples consist of both coarse grains (CG) and fine grains (FG). It is worth noting that the grain size remains unchanged after annealing at different temperatures. However, after annealing treatments at 300 °C, 6 h and 325 °C/6 h, the second phases with different sizes in the matrix become more clearer, and the size of the second phases in the later temper obviously increases.

The sizes of $Al_3(Sc,Zr)$ precipitates in SLM alloys in different states are shown in Table 1. The particle size of $Al_3(Sc,Zr)$ rises gradually with the increase of annealing temperature. The maximum size of the precipitates in the SLM state is 0.15 μm, but the average size is only 0.05 μm. Aftre annealing of 325 °C, 6 h, the size of the precipitates increases sharply, and the average size reaches 0.12 μm.

Figures 3 and 4 show the alloy element map

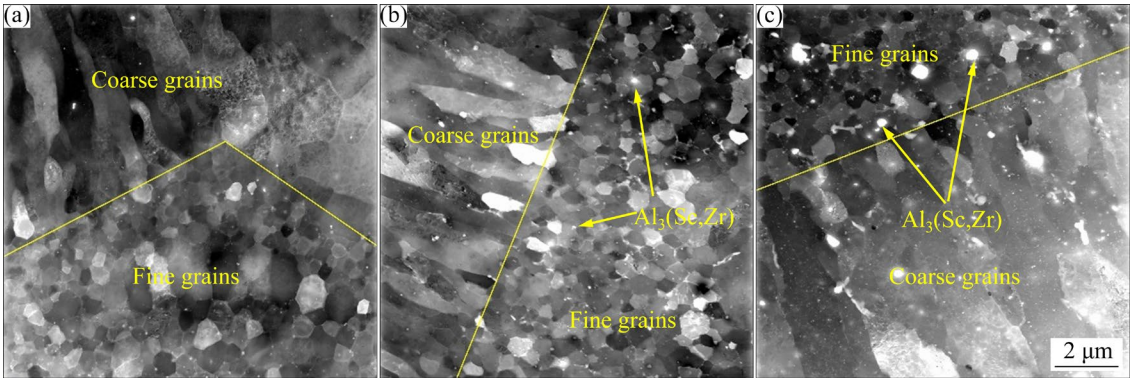

Fig. 2 STEM images of SLM and different-temperature-annealed alloys: (a) SLM; (b) 300 °C, 6 h; (c) 325 °C, 6 h

Table 1 Sizes of $Al_3(Sc,Zr)$ in SLM alloys in different states

State	Biggest size/μm	Smallest size/μm	Average size/μm
SLM	0.15	0.02	0.05
300 °C, 6 h	0.19	0.05	0.09
325 °C, 6 h	0.41	0.05	0.12

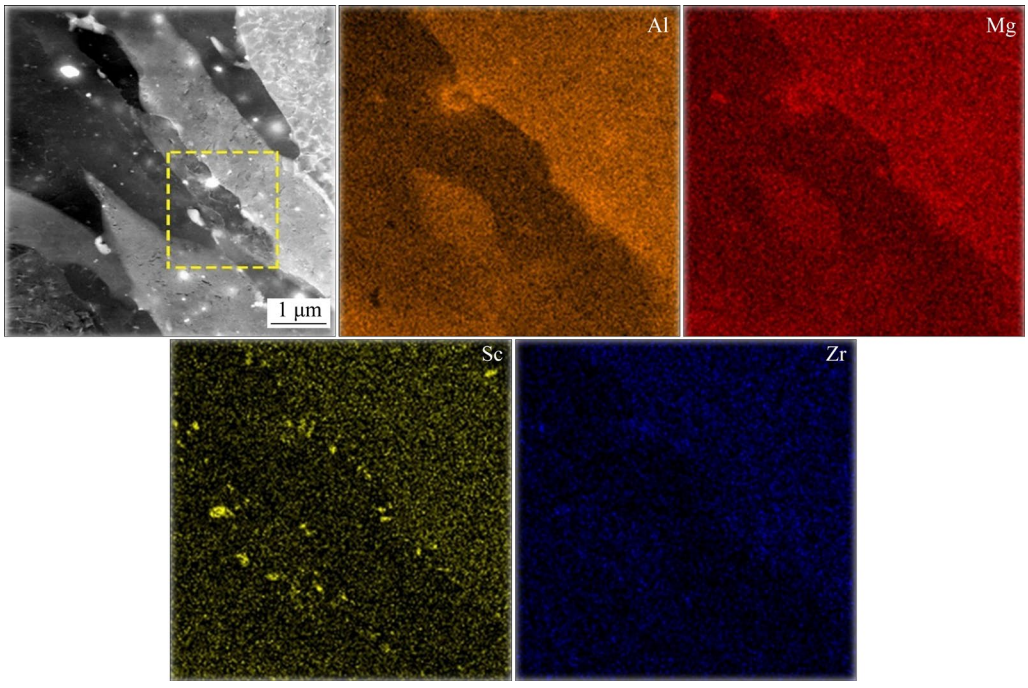

Fig. 3 Map scanning of SLM alloy after annealing at 300 °C for 6 h

scan distribution of the SLM alloy after annealing of 300 °C, 6 h and 325 °C, 6 h, respectively. It can be seen that after annealing of 300 °C, 6 h, the second phases, which is mainly comprised of Al and Sc elements, are obviously precipitated at the grain boundary. After annealing of 325 °C, 6 h, the size of the second phase increases, and its composition is mainly comprised of Al, Sc and Zr. Other alloying elements (especially Mg element) are evenly distributed in the matrix.

High-resolution TEM (HRTEM) along the [001] orientation was used to observe the Al_3Zr particles in the alloy annealed at 325 °C, as shown in Fig. 5. Many Al_3Zr particles with different sizes are distributed on the grain boundaries, as shown in Fig. 5(a). In addition, it can be seen that the Al_3Zr particles significantly coarsen and maintain an incoherent relationship with the matrix, as shown in Fig. 5(b).

3.3 EBSD test

Figure 6 shows the IPF diagrams of the alloy in SLM state and annealing states. It can be seen that the grain morphology of the alloys in different

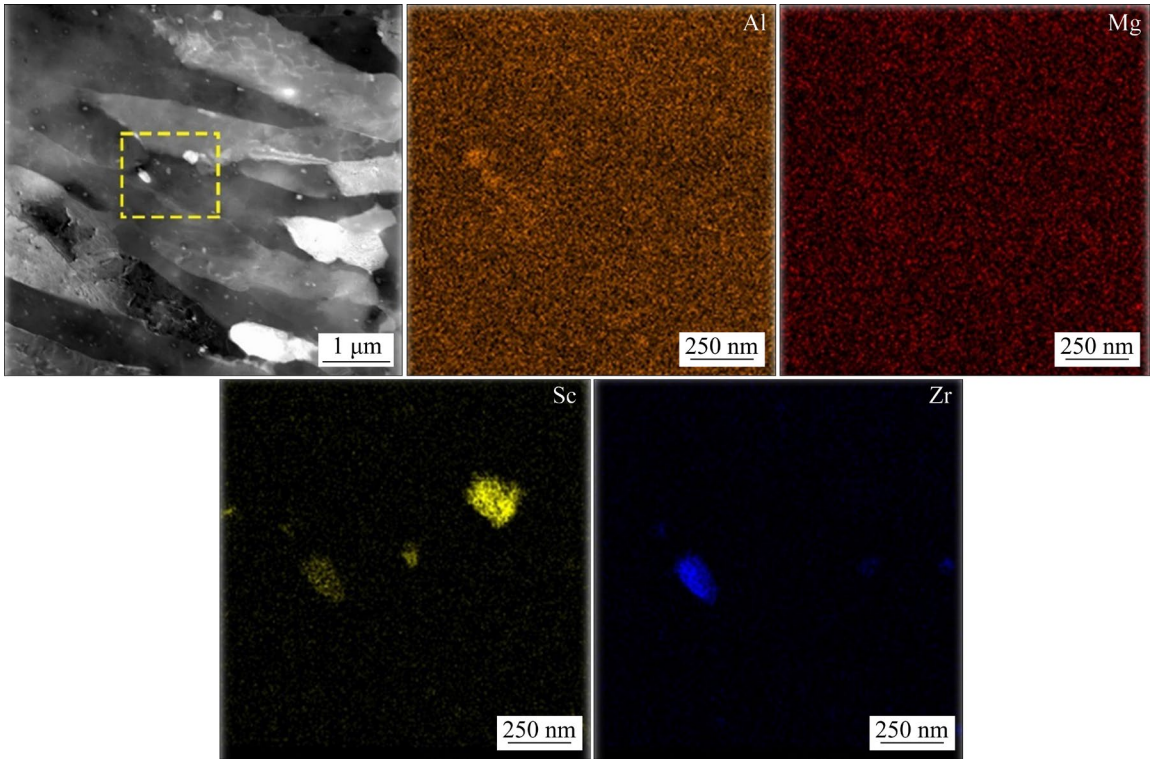

Fig. 4 Map scanning of SLM alloy after annealing at 325 °C for 6 h

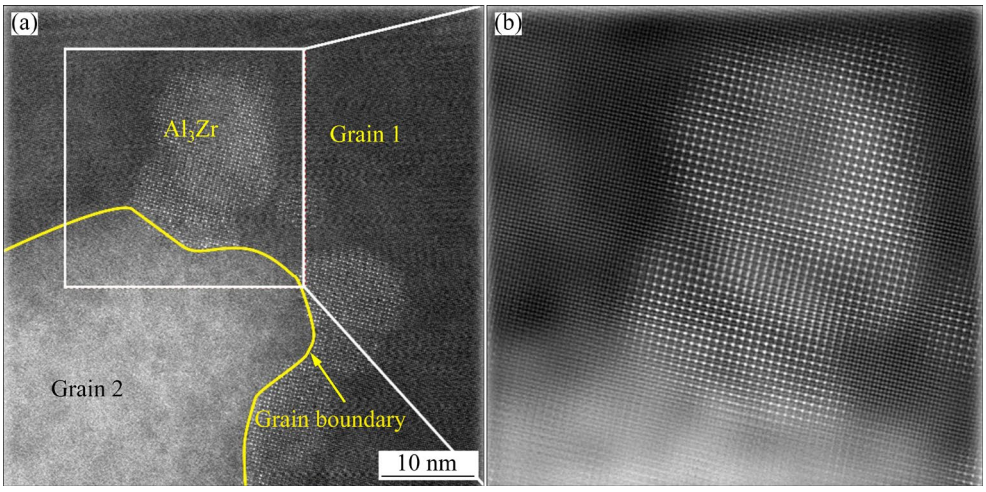

Fig. 5 HRTEM images of Al_3Zr precipitates along [001] of 325 °C, 6 h annealed alloy: (a) HRTEM; (b) Inverse FFT

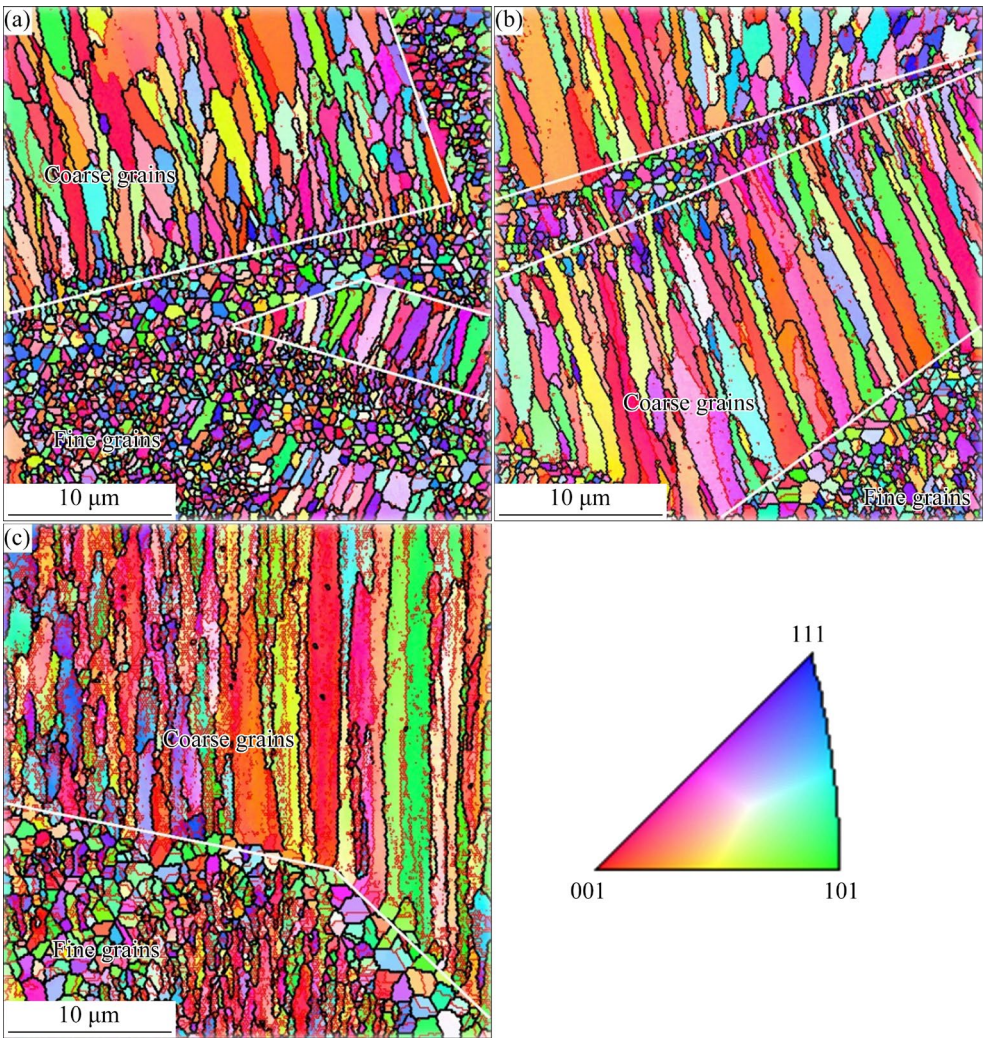

Fig. 6 IPF diagrams of SLM and different-temperature-annealed alloys: (a) SLM; (b) 300 °C, 6 h; (c) 325 °C, 6 h

states is still mainly composed of coarse grains and fine grains, and the grain sizes of coarse and fine grains do not change significantly after annealing. In addition, the color difference between adjacent crystal grains in the FG region is relatively large, which indicates that the crystal grains have different orientations. In contrast, the color difference between adjacent crystal grains in the CG region is small, indicating an obviously preferred orientation.

Figure 7 shows the grain size distribution diagrams of FGs and pole diagrams for the CG and FG regions in the SLM state and different annealing states. The grain sizes of the FG regions in the alloys seem to be less than 2 μm and would not significantly grow with the increase of annealing temperature. The (001) pole figures of the CG and FG regions show that there is a clearly random grain orientation in the FG regions, while preferential grain orientation appears in the CG regions. In addition, with the increase of annealing temperature, the ⟨001⟩ texture intensity of the FG regions and the CG regions increase gradually, which reaches 5.8 and 19.5, respectively after annealing at 325 °C, 6 h.

3.4 Mechanical properties

Table 2 shows the mechanical properties of SLM alloys in different states. It can be clearly seen that the ultimate tensile strength (UTS) and yield strength (YS) of the alloy after annealing at 300 °C for 6 h reach the maximum, which are 518 MPa and 505 MPa, respectively. However, its elongation (13%) is significantly lower than that of SLM alloy. After annealing at 325 °C for 6 h, the UTS, YS and elongation of the alloy are 513 MPa, 483 MPa, and 14.8%, respectively.

Figure 8 shows the tensile fracture diagrams of the SLM alloy at different states. It can be seen

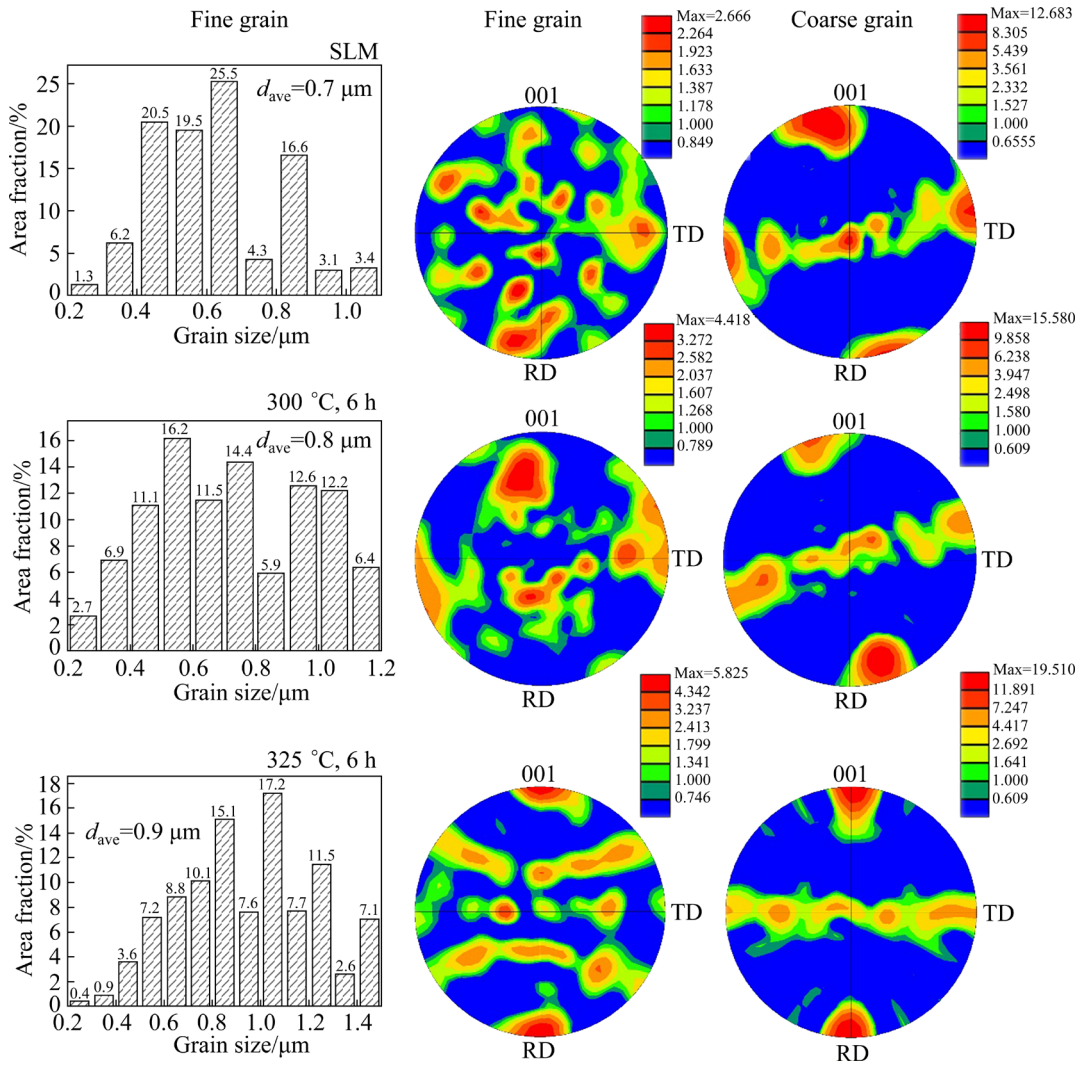

Fig. 7 Grain size diagrams of FGs and pole diagrams of CGs and FGs under SLM state and different annealing states

Table 2 Mechanical properties of SLM alloys in different states

State	UTS/MPa	YS/MPa	Elongation/%
SLM	339	213	24
300 °C, 6 h	518	505	13
325 °C, 6 h	513	483	14.8

that the fracture mode of the alloys could be basically recognized as ductile fracture, where a large number of dimples could be observed in each state. In addition to the dimples, some holes can be also observed. During the SLM forming process, when the laser sweeps through the powder bed, the powder quickly melts and solidifies, and the gas in the solution has no time to escape. The fluid force tends to balance with the vapor pressure in the hole, causing the collapse of liquid metal, and leading to the formation of holes.

4 Discussion

4.1 Effect of annealing temperature on alloy grains

During the SLM forming process, the laser scans the metal powder, and a series of complex physical and chemical phenomena occur during the rapid melting and solidification process, such as absorption and scattering of laser energy, heat transfer, phase change, and melt flow in the molten pool. When the solution is overheated, there is a thermal gradient, which means that uniform nucleation could hardly happen in the alloy. The structure and properties of SLM-formed Al alloy can be adjusted by controlling the grain size and morphology as well as the component and size of these phases. The temperature gradient G and the

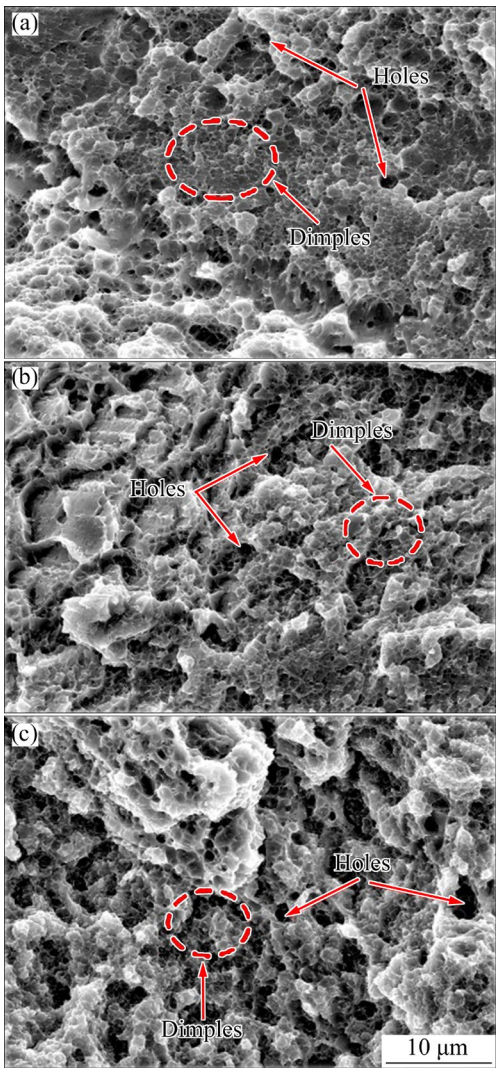

Fig. 8 Room temperature tensile fracture morphologies of SLM alloy in different states: (a) SLM; (b) 300 °C, 6 h; (c) 325 °C, 6 h

solidification rate R affect the grain type and size. $G\times R$ and G/R control the grain size and type, respectively [20]. The larger the $G\times R$, the higher the degree of subcooling in the solution and the finer the crystal grains. With the increase of the G/R ratio, the structure morphology changes to be equiaxed crystals, cellular dendrites and columnar crystals. During the SLM forming process, the Gaussian distribution of laser energy causes the temperature gradient, crystallization speed and subcooling distribution differences in different areas of the molten pool. At the boundary of the molten pool, the value of G is large and the value of R is small, so equiaxed crystals are easy to form. As the grains grow toward the center of the molten pool, the value of G gradually decreases, and the value of R increases, and therefore columnar crystals form, as shown in Fig. 6 [21]. However, the $G\times R$ value is higher at the center of the molten pool, and a small number of equiaxed crystals will also be found. In the FG region, the color difference of adjacent grains is small, which indicates that the difference in crystal grain orientation is small. However, in the CG region, the orientation difference between the adjacent crystal grains is relatively large, and there is an obvious preferred orientation, as shown in Fig. 7. The ⟨100⟩ texture was found in the CG region possessing the largest texture strength of about 11.8.

Usually, when the SLM alloy is annealed in the later stage, the grains will grow to different degrees due to the various annealing temperature. The fine grains obtained through the SLM procedure would merge with each other if the temperature increases in the subsequent annealing process. Grown grains are achieved by the migration of grain boundaries, and the growth rate of grains is proportional to the temperature. The higher the annealing temperature, the faster the growth rate of grains. In addition, as the grains merge and grow, the orientation of the crystal grains will also change. However, the temperature is not high enough to promote the grain growth. Therefore, the grain size and orientation do not change significantly, as shown in Figs. 6 and 7.

4.2 Effect of annealing temperature on second phase particles

Elements such as Sc and Zr in the supersaturated solid solution may be precipitated in the form of nano-precipitated $Al_3(Sc,Zr)$ phases during the low-temperature annealing process, accounting for the effect of precipitation strengthening [22]. As shown in Table 2, the strength of the alloy after annealing treatment increases significantly. It is mainly attributed to the increase in size of $Al_3(Sc,Zr)$ particles. The high annealing temperature can increase the thermal agitation of the atoms and make them more active, enable them to diffuse through dislocations and thus become channels for solute atoms to move, finally resulting in the growth of $Al_3(Sc,Zr)$ particles. And the higher the temperature, the larger the size. The coarsening rate of particles can be described by LSW or KV models [23−25]:

$$r^3 - r_0^3 = K(t - t_0) \quad (1)$$

where r and r_0 are the average radius of the particles at time t and t_0, respectively, K is the coarsening rate of the particle, and r_0 is the initial radius of the particle. As shown in Fig. 3, as the annealing temperature increased to 325 °C, the $Al_3(Sc,Zr)$ particles became significantly larger. According to Eq. (1), when the annealing time is the same, the size of $Al_3(Sc,Zr)$ particles annealed at 325 °C is larger, indicating that the coarsening rate of the particles accelerates with increasing temperature.

4.3 Effect of microstructure on mechanical properties

The improvement of mechanical properties of Al−Mg−Mn−Sc−Zr alloy produced by SLM is mainly attributed to two aspects: the grain size, and the number and size of nano-sized $Al_3(Sc,Zr)$ precipitates. Firstly, the combination of the coarse and fine grains in the SLM alloy exhibits prominent strength and ductility simultaneously during the deformation process [26,27]. Among them, the coarse grains can accommodate more dislocations and lead to high tensile ductility, while the superior strength mainly comes from the fine grains that are not easily deformed, which can withstand more stress than the coarse ones. This is because the grain boundaries can effectively hinder the movement of dislocations. The effect of grain size on yield strength can be described by the Hall−Petch formula [28]:

$$\sigma_y=\sigma_0+kd^{-1/2} \tag{2}$$

where σ_y is the yield strength, σ_0 is the friction stress, k is the experimental constant, and d is the average grain radius. The k value varies from 0.15 to 0.2 $MPa\cdot m^{1/2}$ for Al−(3−6)%Mg alloy [29−31]. Based on Eq. (2), the yield strength of the alloy is supposed to decrease with the increasing grain size. However, after annealing at different temperatures, the strength of the SLM alloy increases first and then decreases as shown in Table 2, while there is no significant change in the grain size after annealing at different temperatures (Figs. 6 and 7). This proves that the grain size is not the main reason for the change of alloy strength.

It can be seen from Fig. 2 that after annealing at different temperatures, $Al_3(Sc,Zr)$ particles have significantly precipitated and grown up, whose strengthening effect is mainly reflected in the grain refinement strengthening and precipitation strengthening [32,33]. The refinement strengthening comes from the pinning effect of $Al_3(Sc,Zr)$ particles on the grain boundaries which inhibits the occurrence of grain growth (Fig. 5). The precipitation strengthening is mainly reflected in the pinning of dislocations by $Al_3(Sc,Zr)$ particles. The pinning effect of $Al_3(Sc,Zr)$ on dislocations is related to its size and density, where the pinning force is called Zener force that can be expressed as [34,35]

$$P_z=\frac{3f_v\gamma_{GB}}{2r} \tag{3}$$

where r is the particle radius, f_v is the volume fraction of the particle, γ_{GB} is the grain boundary energy between the recrystallized core and the deformed region, about 0.3 J/m^2. The smaller the particle size, the larger the volume fraction and the stronger the pinning force. However, the strengthening mechanism of $Al_3(Sc,Zr)$ on the alloy is closely related to its size. When $Al_3(Sc,Zr)$ particles grow up to a certain extent with increasing temperature, the interaction mechanism between $Al_3(Sc,Zr)$ and dislocations may change from dislocation shear mechanism to Orowan bypass mechanism [36]. When the size of $Al_3(Sc,Zr)$ is small, dislocations may interact with the particles in a cut-through manner. In this case, the contribution to the yield strength can be expressed as [37]

$$\Delta\sigma_A=c_1f^m r^n \tag{4}$$

where c_1, m and n are constants; f and r are the volume fraction and radius of precipitates, respectively. It can be seen from Eq. (4) that when the size of $Al_3(Sc,Zr)$ is smaller, the strength of the alloy increases with the rising size. This is because when dislocations shear the $Al_3(Sc,Zr)$ particles, higher stress is required, and thus effectively hinders the movement of the dislocation, leading to the rising strength. When the $Al_3(Sc,Zr)$ particles increase to a certain size, the particles cannot be sheared by dislocations, but bypassed by them instead. The yield strength can be described as [38]

$$\Delta\sigma_B=c_2f^{1/2}r^{-1} \tag{5}$$

where c_2 is a constant. It can be seen from Eq. (5) that as the radius of $Al_3(Sc, Zr)$ increases, the yield strength of the alloy decreases.

As shown in Figs. 3 and 4, as the annealing temperature increases, the radius of $Al_3(Sc,Zr)$ particles increases. When the annealing temperature

rises to 325 °C, the strength of the alloy decreases and the elongation increases, as shown in Table 2. The main strengthening mechanism changes to the Orowan bypass mechanism during the deformation process, owing to the increasing radius of Al_3(Sc,Zr) particles. Under this condition, the required stress for dislocation movement decreases, which results in the strength reduction. Therefore, the main strengthening of SLM alloy after annealing at a certain temperature comes from precipitation strengthening.

5 Conclusions

(1) The tensile strength, yield strength and elongation of Al−3.51Mg−0.42Mn−0.76Sc−0.40Zr alloy at SLM state are 339 MPa, 213 MPa and 24%, respectively. After annealing, the strength of the alloy increases significantly and the elongation decreases. The tensile strength, yield strength and elongation of the alloy annealed at 300 °C for 6 h are 518 MPa, 505 MPa and 13%, respectively.

(2) During the annealing process, the grain morphology and size of the alloy barely change, the segregation of Mg is basically eliminated, and Al_3(Sc,Zr) particles are precipitated from the supersaturated solid solution at the SLM state. As the annealing temperature increases, the size of precipitated Al_3(Sc,Zr) particles increases.

(3) During the annealing process, Al_3(Sc,Zr) particles are generated from the supersaturated solid solution, which is the main reason for the significant strengthening of the alloy.

CRediT authorship contribution statement

Yao LI: Experiment, Writing − Original draft; **Guo-fu XU:** Supervision; **Xiao-yan PENG:** Methodology, Writing − Review & editing; **Ying DENG:** Resources, Data curation; **Zhi-minYIN:** Methodology.

Declaration of competing interest

The authors declare that they have no known competing financial interests or personal relationships that could have appeared to influence the work reported in this paper.

Acknowledgments

This work was financially supported by the National Key Research and Development Program of China (No. 2018YFB2001801), State's Key Project of Research and Development Plan (No. 2021YFC1910505), and the Key Research and Development Program of Guangdong Province, China (No. 2020B010186002).

References

[1] LOUVIS E, FOX P, SUTCLIFFE C J. Selective laser melting of aluminium components [J]. Journal of Materials Processing Technology, 2011, 211(2): 275−284.

[2] ZHANG J L, SONG B, WEI Q S, BOURELL D, SHI Y S. A review of selective laser melting of aluminum alloys: Processing, microstructure, property and developing trends [J]. Journal of Materials Science & Technology, 2019, 35(2): 270−284.

[3] OLAKANMI E O, COCHRANE R F, DALGARNO K W. A review on selective laser sintering/melting (SLS/SLM) of aluminium alloy powders: Processing, microstructure, and properties [J]. Progress in Materials Science, 2015, 74: 401−477.

[4] WANG M, SONG B, WEI Q S, ZHANG Y J, SHI Y S. Effects of annealing on the microstructure and mechanical properties of selective laser melted AlSi7Mg alloy [J]. Materials Science and Engineering A, 2019, 739: 463−472.

[5] BI J, LEI Z L, CHEN Y B, CHEN X, QIN X K, TIAN Z. Effect of process parameters on formability and surface quality of selective laser melted Al−Zn−Sc−Zr alloy from single track to block specimen [J]. Optics & Laser Technology, 2019, 118: 132−139.

[6] GAO C D, YAO M, LI S, FENG P, PENG S P, SHUAI C J. Highly biodegradable and bioactive Fe−Pd-bredigite biocomposites prepared by selective laser melting [J]. Journal of Advanced Research, 2019, 20: 91−104.

[7] XIONG W, HAO L, LI Y, TANG D N, CUI Q, FENG Z Y, YAN C Z. Effect of selective laser melting parameters on morphology, microstructure, densification and mechanical properties of supersaturated silver alloy [J]. Materials & Design, 2019, 170: 107697.

[8] KANNAN C, RAMANUJAM R. Comparative study on the mechanical and microstructural characterisation of AA 7075 nano and hybrid nanocomposites produced by stir and squeeze casting [J]. Journal of Advanced Research, 2017, 8(4): 309−319.

[9] BI J, ZHAO C C, DU B, GUO Q B, DONG G J. Formability and strengthening mechanism of AA6061 tubular components under solid granule medium internal high pressure forming [J]. Transactions of Nonferrous Metals Society of China, 2018, 28(2): 226−234.

[10] GOSTARIANI R, BAGHERPOUR E, RIFAI M, EBRAHIMI R, MIYAMOTO H. Fabrication of Al/AlN in-situ nanocomposite through planetary ball milling and hot extrusion of Al/BN: Microstructural evaluation and mechanical behavior [J]. Journal of Alloys and Compounds, 2018, 768: 329−339.

[11] HEIDARI A, FOROUZAN M R. Optimization of cold rolling process parameters in order to increasing rolling speed limited by chatter vibrations [J]. Journal of Advanced Research, 2013, 4(1): 27−34.

[12] ZHANG L C, KLEMM D, ECKERT J, HAO Y L,

SERCOMBE T B. Manufacture by selective laser melting and mechanical behavior of a biomedical Ti−24Nb−4Zr−8Sn alloy [J]. Scripta Materialia, 2011, 65(1): 21−24.

[13] LIU Y J, LIU Z, JIANG Y, WANG G W, YANG Y, ZHANG L C. Gradient in microstructure and mechanical property of selective laser melted AlSi10Mg [J]. Journal of Alloys and Compounds, 2018, 735: 1414−1421.

[14] JIA Q B, ROMETSCH P, KÜRNSTEINER P, CHAO Q, HUANG A J, WEYLAND M, BOURGEOIS L, WU X H. Selective laser melting of a high strength Al−Mn−Sc alloy: Alloy design and strengthening mechanisms [J]. Acta Materialia, 2019, 171: 108−118.

[15] CHEN B, MOON S K, YAO X, BI G, SHEN J, UMEDA J, KONDOH K. Strength and strain hardening of a selective laser melted AlSi10Mg alloy [J]. Scripta Materialia, 2017, 141: 45−49.

[16] MA R L, PENG C Q, CAI Z Y, WANG R C, ZHOU Z H, LI X G, CAO X Y. Effect of bimodal microstructure on the tensile properties of selective laser melt Al−Mg−Sc−Zr alloy [J]. Journal of Alloys and Compounds, 2020, 815: 152422.

[17] WANG Z H, LIN X, KANG N, HU Y L, CHEN J, HUANG W D. Strength−ductility synergy of selective laser melted Al−Mg−Sc−Zr alloy with a heterogeneous grain structure [J]. Additive Manufacturing, 2020, 34: 101260.

[18] SHI Y J, ROMETSCH P, YANG K, PALM F, WU X H. Characterisation of a novel Sc and Zr modified Al−Mg alloy fabricated by selective laser melting [J]. Materials Letters, 2017, 196: 347−350.

[19] ZHANG J L, GAO J B, SONG B, ZHANG L J, HAN C J, CAI C, ZHOU K, SHI Y S. A novel crack-free Ti-modified Al−Cu−Mg alloy designed for selective laser melting [J]. Additive Manufacturing, 2021, 38: 101829.

[20] YANG K, SHI Y J, PALM F, WU X H, ROMETSCH P. Columnar to equiaxed transition in Al−Mg(−Sc)−Zr alloys produced by selective laser melting [J]. Scripta Materialia, 2018, 145: 113−117.

[21] KIMURA T, NAKAMOTO T. Microstructures and mechanical properties of A356 (AlSi7Mg0.3) aluminum alloy fabricated by selective laser melting [J]. Materials & Design, 2016, 89: 1294−1301.

[22] DAVYDOV V G, ROSTOVA T D, ZAKHAROV V V, FILATOV Y A, YELAGIN V I. Scientific principles of making an alloying addition of scandium to aluminium alloys [J]. Materials Science and Engineering A, 2000, 280(1): 30−36.

[23] ZHANG Y, GAO K Y, WEN S P, HUANG H, NIE Z R, ZHOU D J. The study on the coarsening process and precipitation strengthening of Al_3Er precipitate in Al−Er binary alloy [J]. Journal of Alloys and Compounds, 2014, 610: 27−34.

[24] KARNESKY R A, DUNAND D C, SEIDMAN D N. Evolution of nanoscale precipitates in Al microalloyed with Sc and Er [J]. Acta Materialia, 2009, 57(14): 4022−4031.

[25] LI H Y, BIN J, LIU J J, GAO Z H, LU X C. Precipitation evolution and coarsening resistance at 400 °C of Al microalloyed with Zr and Er [J]. Scripta Materialia, 2012, 67(1): 73−76.

[26] RAEISINIA B, SINCLAIR C W, POOLE W J, TOMÉ C N. On the impact of grain size distribution on the plastic behaviour of polycrystalline metals [J]. Modelling and Simulation in Materials Science and Engineering, 2008, 16(2): 025001.

[27] WITKIN D, LEE Z, RODRIGUEZ R, NUTT S, LAVERNIA E. Al−Mg alloy engineered with bimodal grain size for high strength and increased ductility [J]. Scripta Materialia, 2003, 49(4): 297−302.

[28] GRIFFITHS S, ROSSELL M D, CROTEAU J, VO N Q, DUNAND D C, LEINENBACH C. Effect of laser rescanning on the grain microstructure of a selective laser melted Al−Mg−Zr alloy [J]. Materials Characterization, 2018, 143: 34−42.

[29] HASEGAWA H, KOMURA S, UTSUNOMIYA A, HORITA Z, FURUKAWA M, NEMOTO M, LANGDON T G. Thermal stability of ultrafine-grained aluminum in the presence of Mg and Zr additions [J]. Materials Science and Engineering: A, 1999, 265(1/2): 188−196.

[30] HUSKINS E L, Cao B, RAMESH K T. Strengthening mechanisms in an Al−Mg alloy [J]. Materials Science and Engineering: A, 2010, 527(6): 1292−1298.

[31] DUBYNA A, MOGUCHEVA A, KAIBYSHEV R. Hall-Petch relationship in an Al−Mg−Sc alloy subjected to ECAP [J]. Advanced Materials Research, 2014, 922: 120−125.

[32] DENG Y, YIN Z M, ZHAO K, DUAN J Q, HE Z B. Effects of Sc and Zr microalloying additions on the microstructure and mechanical properties of new Al−Zn−Mg alloys [J]. Journal of Alloys and Compounds, 2012, 530: 71−80.

[33] DENG Y, XU G F, YIN Z M, LEI Q F, HUANG J W. Effects of Sc and Zr microalloying additions on the recrystallization texture and mechanism of Al−Zn−Mg alloys [J]. Journal of Alloys and Compounds, 2013, 580: 412−426.

[34] WU H, WEN S P, WU X L,GAO K Y, HUANG H, WANG W, NIE Z R. A study of precipitation strengthening and recrystallization behavior in dilute Al−Er−Hf−Zr alloys [J]. Materials Science and Engineering A, 2015, 639: 307−313.

[35] WU H, WEN S P, HUANG H, LI B L, WU X L, GAO K Y, WANG W, NIE Z R. Effects of homogenization on precipitation of $Al_3(Er,Zr)$ particles and recrystallization behavior in a new type Al−Zn−Mg−Er−Zr alloy [J]. Materials Science and Engineering A, 2017, 689: 313−322.

[36] MA K K, WEN H M, HU T, TOPPING T D, ISHEIM D, SEIDMAN D N, LAVERNIA E J, SCHOENUNG J M. Mechanical behavior and strengthening mechanisms in ultrafine grain precipitation-strengthened aluminum alloy [J]. Acta Materialia, 2014, 62: 141−155.

[37] LIU Y, JIANG D M, LI B Q, YANG W S, HU J. Effect of cooling aging on microstructure and mechanical properties of an Al−Zn−Mg−Cu alloy [J]. Materials & Design, 2014, 57: 79−86.

[38] LI Y, XU G F, PENG X Y, WANG F X, LIANG X P. Effect of different aging treatment on high temperature properties of die-forged Al−5.87Zn−2.07Mg−2.42Cu alloy [J]. Materials Characterization, 2020, 164: 110239.

经不同温度退火处理的选区激光熔化 Al−Mg−Mn−Sc−Zr 合金的显微组织和力学性能

李 耀[1]，徐国富[1,2]，彭小燕[1,2]，邓 英[1,2]，尹志民[1,2]

1. 中南大学 材料科学与工程学院，长沙 410083；
2. 中南大学 有色材料科学与工程教育部重点实验室，长沙 410083

摘 要：采用选区激光熔化(SLM)法制备 Al−3.51Mg−0.42Mn−0.76Sc−0.40Zr(质量分数，%)合金，并研究该合金经 300 ℃，6 h 和 325 ℃，6 h 退火处理后的力学性能和显微组织。SLM 态合金的抗拉强度、屈服强度和伸长率分别为 339 MPa、213 MPa 和 24%。经 300 ℃，6 h 退火处理后，合金的抗拉强度和屈服强度分别提高至 518 MPa 和 505 MPa，伸长率下降至 13%；而经 325 ℃，6 h 退火处理后，合金的屈服强度降低至 483 MPa。合金经 300 ℃，6 h 和 325 ℃，6 h 退火处理后晶粒没有明显长大，但 Mg 元素的偏聚明显减少；纳米级 Al_3(Sc,Zr)相从合金基体中析出，且其平均尺寸随退火温度升高而有所增大。因此，退火态 SLM 铝合金强度的提高主要归因于 Al_3(Sc,Zr)的析出强化，且强化机制主要为位错切过机制。当退火温度过高时，Al_3(Sc,Zr)粒子发生粗化从而引起强度下降。

关键词：Al−Mg−Mn−Sc−Zr 合金；选区激光熔化；退火温度；显微组织；力学性能

(Edited by Sai-qian YUAN)